ARTICLES
PUBLISHED ONLINE: 20 MARCH 2017 | DOI: 10.1038/NMAT4878

nature materials

# Functional electronic inversion layers at ferroelectric domain walls

J. A. Mundy[1†], J. Schaab[2†], Y. Kumagai[2†], A. Cano[3], M. Stengel[4,5], I. P. Krug[6], D. M. Gottlob[7], H. Doğanay[7], M. E. Holtz[1], R. Held[8], Z. Yan[9,10], E. Bourret[9], C. M. Schneider[7], D. G. Schlom[8,11], D. A. Muller[1,11], R. Ramesh[9,12], N. A. Spaldin[2] and D. Meier[2,13]*

**Ferroelectric domain walls hold great promise as functional two-dimensional materials because of their unusual electronic properties. Particularly intriguing are the so-called charged walls where a polarity mismatch causes local, diverging electrostatic potentials requiring charge compensation and hence a change in the electronic structure. These walls can exhibit significantly enhanced conductivity and serve as a circuit path. The development of all-domain-wall devices, however, also requires walls with controllable output to emulate electronic nano-components such as diodes and transistors. Here we demonstrate electric-field control of the electronic transport at ferroelectric domain walls. We reversibly switch from resistive to conductive behaviour at charged walls in semiconducting $ErMnO_3$. We relate the transition to the formation—and eventual activation—of an inversion layer that acts as the channel for the charge transport. The findings provide new insight into the domain-wall physics in ferroelectrics and foreshadow the possibility to design elementary digital devices for all-domain-wall circuitry.**

Recently, ferroelectric domain walls have been demonstrated to develop novel electronic ground states that differ from those of the surrounding bulk material. In addition, they can be induced, moved and erased on demand, representing natural, flexible interfaces with novel functional properties[1–3]. After the seminal discovery of electrically conducting walls in the multiferroic semiconductor $BiFeO_3$ (ref. 4), there have been numerous reports on conducting walls in prototypical ferroelectrics including $PbZr_{0.2}Ti_{0.8}O_3$ (ref. 5), $LiNbO_3$ (ref. 6) and $BaTiO_3$ (ref. 7), as well as improper ferroelectrics such as hexagonal $R$MnO$_3$(R = Sc, Y, In, Dy to Lu)[8,9] and $(Ca,Sr)_3Ti_2O_7$ (ref. 10), indicating that such conductivity is a general phenomenon[2,3,11,12]. Conducting domain walls are now anticipated in a wide range of otherwise insulating ferroic materials, with the observation of metallic domain walls in the magnetic insulator $Nd_2Ir_2O_7$ being a major new development[13]. Furthermore, recently established characterization methods allow one to determine intrinsic domain-wall properties with unprecedented completeness. Local Hall measurements, for instance, reveal the types, mobilities and densities of involved carriers[14], and advanced frequency-dependent[15,16] and contact-free transport[17,18] measurements provide insight into the underlying conduction mechanisms. To make use of the exotic domain-wall properties and ultimately design domain-wall-based devices for nanotechnology, however, additional functionality beyond just conduction is required that allows the behaviour of classical electrical components to be emulated at the nanoscale. Here, we demonstrate electric-field control of the electronic transport at charged head-to-head domain walls in semiconducting $ErMnO_3$. The electric field allows reversible switching between resistive and conductive domain-wall states, corresponding to a domain-wall-based binary switch. We relate this qualitative change in the transport behaviour to the formation—and eventual activation—of an electronic inversion layer at the head-to-head walls that acts as the channel for the charge transport.

For our study we choose the narrow-bandgap, p-type semiconductor $ErMnO_3$ ($E_g = 1.6$ eV; ref. 19) as it naturally develops all fundamental types of ferroelectric domain wall at room temperature ($T_C = 1{,}470$ K; ref. 20), including neutral (side-by-side) as well as negatively (tail-to-tail) and positively charged (head-to-head) wall configurations[8]. Moreover, the atomic structure and basic transport properties of these walls are particularly well understood[8,21,22]. While the main interest in neutral domain walls is associated with their functionality as insulating barriers[23], charged domain walls are intriguing because of their unique electrostatics, giving rise to diverse and tunable electronic transport properties[8]. Enhanced electronic conductance has been reported for tail-to-tail walls in $ErMnO_3$ and explained based on the accumulation of mobile holes[3,14]. The holes originate from interstitial oxygen anions[24] and represent the majority carriers. These carriers accumulate at tail-to-tail walls to screen the local, divergent electric field. Likewise, head-to-head walls in the same sample exhibit suppressed conductance, which has been explained by the depletion of majority carriers, with possible additional contributions from minority carriers (electrons)[8,11]. The latter are particularly interesting, as the involvement of both

[1]School of Applied and Engineering Physics, Cornell University, Ithaca, New York 14853, USA. [2]Department of Materials, ETH Zurich, 8093 Zürich, Switzerland. [3]CNRS, Université de Bordeaux, ICMCB, UPR 9048, 33600 Pessac, France. [4]ICREA—Institució Catalana de Recerca i Estudis Avançats, 08010 Barcelona, Spain. [5]Institut de Ciència de Materials de Barcelona (ICMAB-CSIC), Campus UAB, 08193 Bellaterra, Spain. [6]Institut für Optik und Atomare Physik, TU Berlin, 10623 Berlin, Germany. [7]Peter Grünberg Institute (PGI-6), Forschungszentrum Jülich, 52425 Jülich, Germany. [8]Department of Materials Science and Engineering, Cornell University, Ithaca, New York 14853, USA. [9]Materials Sciences Division, Lawrence Berkeley National Laboratory, Berkeley, California 94720, USA. [10]Department of Physics, ETH Zurich, Otto-Stern-Weg 1, 8093 Zürich, Switzerland. [11]Kavli Institute at Cornell for Nanoscale Science, Ithaca, New York 14853, USA. [12]Department of Materials Science and Engineering and Department of Physics, UC Berkeley, Berkeley, California 94720, USA. [13]Department of Materials Science and Engineering, Norwegian University of Science and Technology, 7491 Trondheim, Norway. †These authors contributed equally to this work. *e-mail: dennis.meier@ntnu.no



© 2017 Macmillan Publishers Limited, part of Springer Nature. All rights reserved.

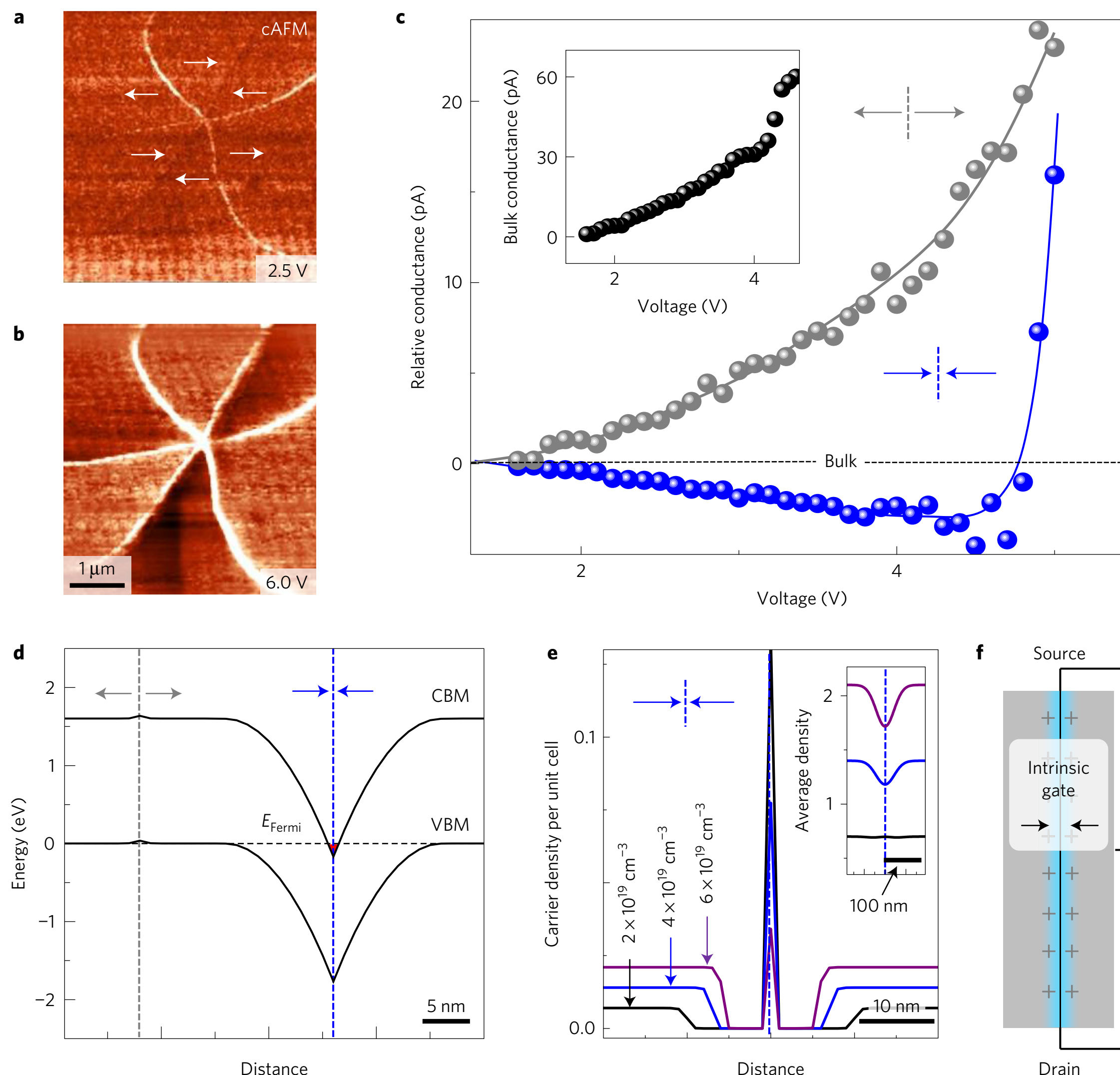


**Figure 1 | Electronic transport and band structure at tail-to-tail and head-to-head walls. a**, cAFM scan obtained at a bias voltage of 2.5 V on $ErMnO_3$ with in-plane polarization as indicated by the white arrows (the orientation corresponds to a *y*-cut with the (110)-direction normal to the sample surface). The image reveals a six-fold meeting point of conducting tail-to-tail (bright) and insulating head-to-head (dark) domain walls. **b**, cAFM image obtained with a bias voltage of 6 V at the same position as shown in **a** with both tail-to-tail and head-to-head walls exhibiting enhanced conductance compared with the bulk. **c**, Relative current–voltage characteristics measured at tail-to-tail and head-to-head walls after subtraction of the bulk current (for reference, the bulk conductance is shown in the inset). See Supplementary Fig. 3 for corresponding spatially resolved data. **d**, Calculated band bending at tail-to-tail and head-to-head domain walls (vertical dashed lines) with arrows indicating the polarization orientation in adjacent domains. Black solid lines correspond to the conduction-band minimum (CBM) and valence-band maximum (VBM) for $p_0 = 2 \times 10^{19}$ cm$^{-3}$ with the horizontal dashed line indicating the Fermi level, $E_{Fermi}$. **e**, Calculated carrier density at head-to-head walls. With increasing hole carrier density the screening by hole depletion becomes more efficient so that the density of electrons decreases. The inset presents the average carrier density. Lines are running averages based on a Gaussian convolution function ($\propto \exp(-x^2/s^2)$, $s = 30$ nm), which corresponds to a realistic spatial resolution when mapping local current by cAFM. **f**, Conceptual sketch of a domain-wall-based field-effect transistor with polarization charges playing the role of the gate.

majority and minority carriers may give rise to novel, functional domain-wall behaviour.

To study emergent domain-wall properties at head-to-head walls in $ErMnO_3$, we measure the local electronic transport over an extended voltage range. Crystals of $ErMnO_3$ were grown by the pressurized floating-zone method[25] and specimens with in-plane polarization and a thickness of ≈1 mm were prepared and chemo-mechanically polished with silica slurry. In Fig. 1a–c we present conductive atomic force microscopy (cAFM) data obtained with a conductive diamond-coated tip (DCP12, NT-MDT) under sample bias voltages of up to 6 V. Test measurements on different walls and with different tip coatings reveal bulk-dominated transport behaviour, ensuring that intrinsic domain-wall properties are probed (see Supplementary Notes and Supplementary Figs 1 and 2). At low bias voltage ($V_{bias} = 2.5$ V) we observe the established transport behaviour[8,9] with conducting tail-to-tail (bright) and insulating head-to-head (dark) domain walls (Fig. 1a). A qualitatively different transport phenomenon, however, arises at higher voltage as shown by the scan in Fig. 1b, taken at $V_{bias} = 6$ V. The spatially resolved data highlight that both tail-to-tail and head-to-head walls can exhibit a higher electronic conductance than the surrounding domains. A more detailed study is shown in Fig. 1c, which is conducted in an area with well-separated walls to exclude crosstalk effects (see Supplementary Fig. 3). Figure 1c shows the relative domain-wall conductance, $\Delta I$, after subtracting the bulk current, which for reference, is shown in the inset to Fig. 1c ($\Delta I = I_{wall} - I_{bulk}$). The comparison with respect to the bulk (black dashed line in Fig. 1c) reveals that the head-to-head domain walls become more conducting than



© 2017 Macmillan Publishers Limited, part of Springer Nature. All rights reserved.

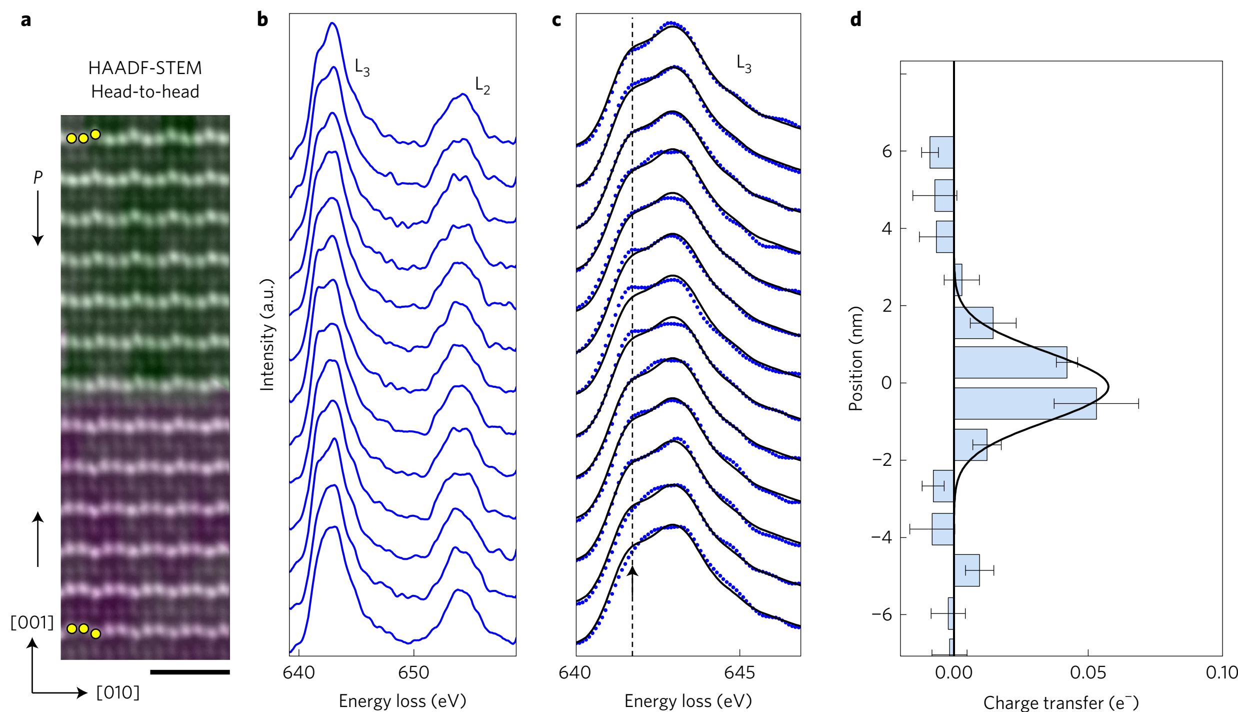


**Figure 2 | Manganese valence change at head-to-head domain walls. a**, HAADF-STEM image of a head-to-head domain wall. The image is coloured to indicate the magnitude and direction of the displacement of erbium atoms with a sharp transition between $+P$ and $-P$ domains ($-P$ domain: down–down–up; $+P$ domain: up-up–down as indicated by yellow circles)[21]. The scale bar is 1 nm. **b**, Layer-by-layer EELS spectra showing the evolution of the Mn $L_{2,3}$ edge across the head-to-head domain wall. **c**, Zoom-in to the $L_3$ edge in **b**. A comparison of the EELS spectra (blue dots) with $Mn^{3+}$ reference data (solid line) reveals a spectral feature around 641 eV (indicated by the dashed line) that occurs in the vicinity of the head-to-head domain wall. **d**, Electron transfer (per manganese atom at the domain wall) to the wall calculated from the local manganese valence measured by EELS. Error bars are the standard error of the mean.

the bulk above $V_c \approx 4.8$ V, approaching the conductance measured at the tail-to-tail walls for $V > V_c$. The transition from resistive ($I_{wall} < I_{bulk}$) to conductive ($I_{wall} > I_{bulk}$) behaviour occurs gradually and for moderate electric fields (see also Supplementary Fig. 2). For comparison, more than one order of magnitude higher electric fields are used to induce domain-wall currents in $BiFeO_3$ or $PbZr_{0.2}Ti_{0.8}O_3$ thin films[4,5]. The low electric-field energy suggests a qualitative change in the electronic transport at head-to-head walls rather than a breakdown of the insulating domain-wall state. This qualitative change, however, cannot be explained based on the depletion of majority carriers (holes) alone.

To better understand this unusual transport phenomenon, we build a density functional theory (DFT)-based semiclassical model describing the redistribution of mobile carriers. Assuming that $ErMnO_3$ behaves like a simple band insulator we solve Poisson's equation self-consistently with the carriers treated semiclassically (see Methods for details) and obtain the band diagram presented in Fig. 1d. We see that far from the domain walls the potential is flat and the Fermi level, $E_{Fermi}$, lies just below the valence-band maximum (VBM) corresponding to a realistic carrier density of $p_0 = 2 \times 10^{19}$ cm$^{-3}$, that is, a doping level of 0.007 holes per unit cell. At the tail-to-tail walls the VBM shifts upwards and generates more holes, which screen the negative bound domain-wall charge, $-2P_z$ ($\mathbf{P} = (0, 0, P_z)$); this is consistent with the enhanced conductance measured at the tail-to-tail domain walls[8,9] (see Fig. 1a). For the head-to-head domain walls, we find a significant band bending with the conduction-band minimum (CBM) dipping below the Fermi energy. This implies that the screening at head-to-head domain walls is realized by both a depletion of holes, occurring in a total range of about 22 nm, and an accumulation of electrons right at the wall where the CBM lies below $E_{Fermi}$ (see Fig. 1d). Thus, the simple model indicates that the density of electrons, that is, the minority carriers, is considerably enhanced at the head-to-head walls. This result is in agreement with previous analytical investigations[11], demonstrating the soundness of our alternative DFT-based approach. In both models, however, hole depletion needs to override the electron accumulation to reproduce the experimental observation of insulating walls for $V < V_c$ (Fig. 1a). This requirement is illustrated in Fig. 1e, where the density of carriers is plotted as a function of the distance from the wall. The corresponding average carrier density—which is proportional to the conductance—is shown in the inset. For $V > V_c$ the electrons probably dominate the domain-wall conductance as they are the only mobile carriers available for charge transport at the head-to-head walls. Aside from the observed change in conductance, the pronounced band bending at head-to-head walls is appealing for the design of domain-wall-based transistors as sketched in Fig. 1f. The field effect associated with the polarization charges can, in principle[8,26], be used to modulate the conductivity at the wall and, hence, serve as a natural, intrinsic gate. In the following, however, we will focus on the voltage-driven transition from resistive to conductive behaviour.

We next use electron energy-loss spectroscopy (EELS) to probe the electronic structure at the head-to-head walls at atomic resolution. Figure 2a shows a high-angle annular dark-field scanning transmission electron microscopy (HAADF-STEM) image of a head-to-head domain wall imaged along the [100] zone axis of $ErMnO_3$ (see Methods for details). The erbium ions are shifted with respect to the manganese–oxygen polyhedra, displaying either an down–down–up ($-P$ domain) or up–up–down ($+P$ domain) arrangement[21]. These displacements indicate the local spontaneous polarization and thus provide a local measure for the polarization reorientation across the head-to-head wall. We find a rather abrupt discontinuity of the polarization orientation at the wall, consistent with previous work[21]. Using spatially resolved EELS we



© 2017 Macmillan Publishers Limited, part of Springer Nature. All rights reserved.

investigate the electrochemical wall structure by measuring the local manganese valence. Figure 2b displays the evolution of the corresponding EELS spectra, taken at the Mn $L_{2,3}$ edge, across the head-to-head wall. Figure 2c shows an enlarged image of the Mn $L_3$ edge where the experimental data points are overlaid with a manganese reference spectrum collected on the $ErMnO_3$ sample away from the domain wall. The spectra collected within the domain areas exhibit minor differences that reflect an inhomogeneity of the electrical background. In the vicinity of the head-to-head wall, we clearly note a distinct feature at ≈641 eV in the spectra. Here, the data are not well described by the $Mn^{3+}$ reference spectrum (see also Supplementary Fig. 4).

To quantify the change observed at the Mn $L_{2,3}$ edge at the head-to-head wall, the full Mn $L_{2,3}$ edge is fitted with two spectra corresponding to the $Mn^{3+}$ and $Mn^{2.8+}$ valence states. The $Mn^{2.8+}$ spectrum is calculated as a linear combination of $Mn^{3+}$ and $Mn^{2+}$ spectra as described in the Supplementary Notes and Supplementary Fig. 5 (we note that the spectrum of six-fold-coordinated $Mn^{2+}$ is used for reference as the current work represents the first spectroscopic study of the $Mn^{2+}$ electronic state in trigonal bipyramidal coordination). The analysis reveals a statistically significant concentration of the lower valence state spatially localized over 2–3 unit cells near the head-to-head domain wall. On the basis of the valence concentration, we calculate the excess charge per manganese atom at the domain wall relative to the $Mn^{3+}$ state in the bulk[27]. This charge as a function of position is plotted in Fig. 2d. Aggregating over several such walls at distinct locations in the material, we find that the local valence change is equivalent to the accumulation of a negative charge of 0.09 ± 0.04 electrons per manganese atom at the head-to-head wall position. Since the bulk polarization[28] of $ErMnO_3$ is ≈6 μC cm$^{-2}$, the amount of negative charge density needed to screen the polar discontinuity at the head-to-head walls is ≈12 μC cm$^{-2}$. This value converts into a carrier density in the order of ≈0.1 (0.3) electrons per manganese ion (unit cell), which is in the range of our experimental uncertainty. Complementary EELS measurements at the oxygen K edge show no statistically relevant anomaly (Supplementary Fig. 5c), excluding that oxygen vacancy formation is responsible for the local manganese valence change. EELS studies at tail-to-tail walls and X-ray photoemission electron microscopy further confirm that the lower valence state is a feature that is unique to the area (2–3 unit cells) around the head-to-head walls (see Supplementary Notes and Supplementary Figs 6–8). In agreement with our semiclassical model, the EELS results corroborate that electron accumulation, in addition to hole depletion, plays an important role for the compensation of the polarity mismatch at head-to-head domain walls in $ErMnO_3$.

To determine the orbital character of the electrons and elucidate the relation between their accumulation and the local manganese valence state, we perform first-principles calculations based on DFT within the local density approximation $+U$ method using $YMnO_3$ as our model hexagonal manganite ($YMnO_3$ is structurally and electronically similar to $ErMnO_3$, and the absence of $f$-electrons simplifies the DFT description). In Fig. 3a we show the calculated orbital-resolved density of states for the valence and conduction bands. We see that, consistent with literature calculations[29,30], the conduction band is narrow because it is formed from localized $d_{z^2}$ orbitals, with only minimal hybridization with neighbouring axial oxygen $p_z$ orbitals, whereas the valence band is broad, consisting of strongly hybridized and delocalized manganese $d$- and oxygen $2p$ states. At the head-to-head walls, where the CBM dips below the Fermi level (Fig. 1d), we therefore expect localized electrons, whereas holes at the VBM are delocalized in nature. This expectation is consistent with our spectroscopy data, indicating a manganese valence change associated with the accumulation of electrons.

While our theoretical analysis gives an appealing qualitative description of our experimental data, at the quantitative level there is

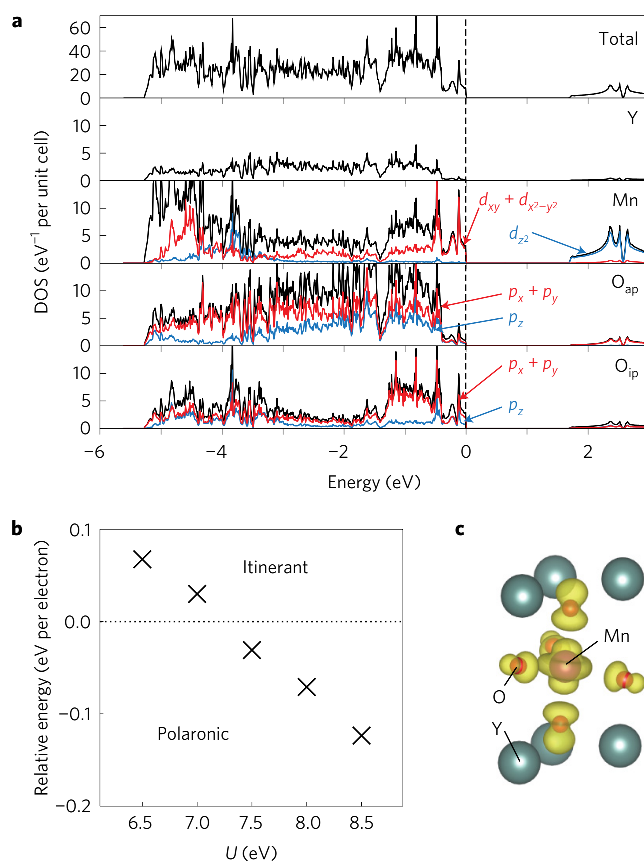


**Figure 3 | Orbital nature of electrons at head-to-head domain walls.** **a**, Orbital-resolved density of states (DOS). The black lines indicate the sum of the local density of states, while the blue and red lines show the contributions from the different orbitals. The black dashed line at 0 eV indicates the Fermi energy. $O_{ap}$ and $O_{ip}$ represent the oxygens located at the apical sites and in-plane sites, respectively, of the MnO-bipyramidal layers. **b**, Calculated relative energy between electronic Bloch and polaron states. Data points (black crosses) above the dashed line indicate that an itinerant Bloch state is stable for the respective $U$ values, whereas data points below the line show that a polaronic state is stabilized. **c**, Illustration of the calculated electronic polaron state.

a discrepancy between the density of electron carriers at the domain wall predicted by the semiclassical model and that indicated by the EELS measurements. According to the cAFM measurements, hole depletion needs to override the electron accumulation in the model, while EELS points to a dominant electron-like compensation. This raises the question of whether an additional mechanism is at play in the hexagonal manganites. The semiclassical model and even our DFT band picture constitute a drastic simplification of the problem, especially in a material such as $ErMnO_3$, where many-body correlation effects probably play an important role. In this context, it is important to recognize that electrons in the spatially localized manganese $d_{z^2}$ orbitals experience a strong on-site Coulombic repulsion, which typically favours the formation of localized polaronic states rather than itinerant Bloch states[31]. To verify whether such a scenario might apply to our case, we calculate the energies of hypothetical polaronic states for both electrons and holes by introducing a single electron or hole in a 120-atom supercell and lowering the local symmetry around a manganese site (see Methods). We find (Fig. 3b) that an isolated electron polaron has lower energy than an itinerant Bloch electron for $U$ values of 7.5 eV and higher. (In contrast, hole polarons remain unstable relative to the Bloch state even for $U$ values as large as 8.5 eV.) At head-to-head domain walls, we expect that polarons arrange



© 2017 Macmillan Publishers Limited, part of Springer Nature. All rights reserved.

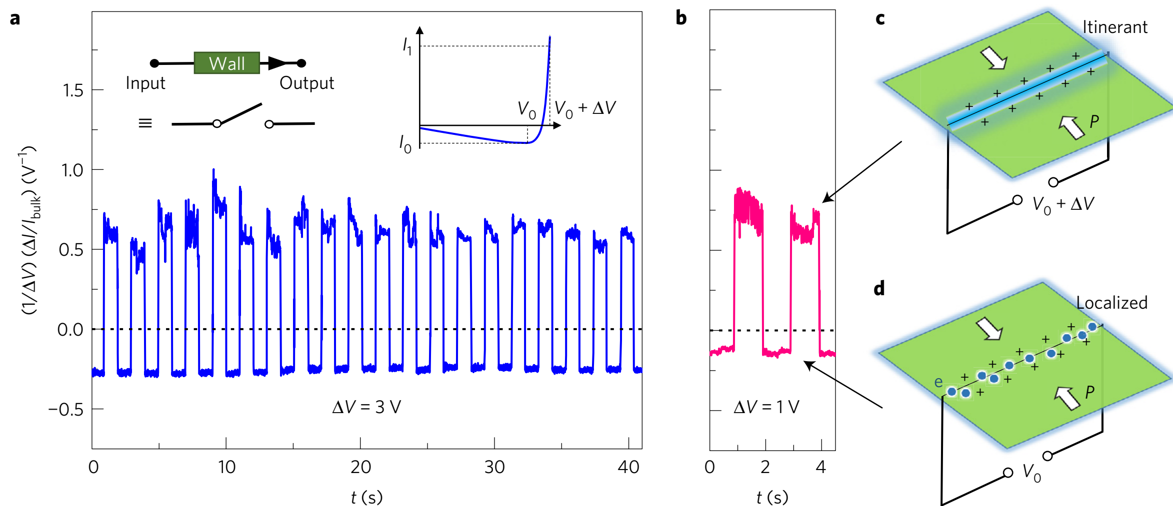


**Figure 4 | Electric-field control of electronic transport at head-to-head domain walls. a**, Normalized domain-wall current measured as a function of time over 20 switching cycles between resistive ($I_0 < I_{bulk}$) and conducting ($I_1 > I_{bulk}$) behaviour. For voltages $V_0 = 2$ V and $\Delta V = 3$ V (see inset to **a** for a schematic illustration), reversible control can be reliably realized for 20 switching cycles, which is the largest number of cycles we investigated. **b**, Enhanced gain can be achieved, for example, by increasing $I_0$, yielding $\Delta I/\Delta V \approx 15$ pA $V^{-1}$ for $V_0 = 4$ V and $\Delta V = 1$ V. The increase in gain, however, requires larger currents, which cause degradation as described in the main text. **c**, Sketch showing the conductive domain-wall state for $V = V_0 + \Delta V$ with itinerant electrons illustrated in blue. **d**, Resistive domain-wall state with localized electrons for $V_0$.

in a two-dimensional lattice, and thereby significantly reduce their formation energy compared with the case of an isolated defect. We find that, by combining this correlation effect with the data of Fig. 3b and our band-bending model (see Supplementary Information), polarons are most likely to form right at the head-to-head wall, for a realistic range of values of both the Hubbard $U$ ($U \approx 6$–6.5 eV) and the bulk doping level. Note that polarons should give an additional barrier to electronic conductivity at low voltage, consistent with the observations presented in Fig. 1, lifting the band-model-related condition that hole depletion dominates over electron accumulation at head-to-head walls (Fig. 1e).

Thus, experiment and theory identify an accumulation of electrons at the head-to-head walls, leading to the formation of an inversion layer. The electrons are in a localized polaronic state and hence do not contribute to the conductance at low voltage. For high voltage ($V > V_c$) these electrons dominate the conductance as they are the only available mobile carriers. In the polaronic picture, $V_c$ is related to the transition from localized to itinerant electrons and hence to the activation of the inversion layer as the effective channel for the domain-wall transport. This behaviour is fundamentally different from the majority-carrier-enabled transport at tail-to-tail domain walls, which does not involve significant lattice coupling[14].

In Fig. 4a,b we show how this behaviour can be used to realize, for example, a domain-wall-based binary switch. The cAFM data in Fig. 4a are collected at a head-to-head wall as a function of time with the bias voltage varying repeatedly between $V_0 = 2$ V and $V_0 + \Delta V = 5$ V. Due to the unusual $I$–$V$ characteristic at the head-to-head wall, the change in electric field allows reversible switching between resistive ($I_0 < I_{bulk}$) and conductive ($I_1 > I_{bulk}$) behaviour as reflected by the normalized domain-wall current $1/\Delta V \cdot (\Delta I/I_{bulk})$ in Fig. 4a. Figure 4b shows that the related electric-field-induced gain, $\Delta I/\Delta V$, can be enhanced by increasing the base voltage $V_0$. The enhancement in gain, however, is accompanied by the flow of a larger current $I_0$, which causes irreversible changes in the electronic surface structure and fast degradation of the domain-wall-based binary switch after only two to three cycles (not shown). Note that the transition from resistive to conductive behaviour reflects a change from hole- to electron-dominated conductance. This qualitative change in the transport behaviour is a unique feature of the inversion layer formed at the head-to-head walls.

The head-to-head domain walls studied in this work thus represent a natural type of semiconducting oxide interface at which the nature of the electronic transport can be manipulated at will and in a fully reversible fashion. This new degree of freedom becomes possible as the local transport behaviour is determined by the interplay between holes and electrons. Now that we have shown that functional inversion layers are formed at charged domain walls, the next step is to utilize individual walls in device-like architectures. In general, an involvement of both minority and majority carries is appealing as it allows device paradigms to be extended into the realm of minority-carrier devices including bistable switches and bipolar transistors. Minority-carrier devices are typically slower, but offer better on-state performance and larger breakdown voltages[32]. With this, our results foreshadow conceptually new domain-wall applications that go beyond spatially mobile, conducting two-dimensional channels. This opportunity brings us an important step closer to the realization of reconfigurable all-domain-wall circuits for next-generation nanotechnology.

## Methods

Methods, including statements of data availability and any associated accession codes and references, are available in the online version of this paper.

Received 26 April 2016; accepted 6 February 2017; published online 20 March 2017

## References

1. Salje, E. K. H. Multiferroic domain boundaries as active memory devices: trajectories towards domain boundary engineering. *Chem. Phys. Chem.* **11,** 940–950 (2010).
2. Catalan, G., Seidel, S., Ramesh, R. & Scott, J. F. Domain wall nanoelectronics. *Rev. Mod. Phys.* **84,** 119–156 (2012).
3. Meier, D. Functional multiferroic domain walls in multiferroics. *J. Phys. Condens. Matter* **27,** 463003 (2015).
4. Seidel, J. *et al*. Conduction at domain walls in oxide multiferroics. *Nat. Mater.* **8,** 229–234 (2009).
5. Maksymovych, P. *et al*. Tunable metallic conductance in ferroelectric nanodomains. *Nano Lett.* **12,** 209–213 (2012).
6. Schröder, M. *et al*. Conducting domain walls in lithium niobate single crystals. *Adv. Funct. Mater.* **22,** 3936–3944 (2012).



© 2017 Macmillan Publishers Limited, part of Springer Nature. All rights reserved.

7. Sluka, T. *et al*. Free-electron gas at charged domain walls in insulating $BaTiO_3$. *Nat. Commun.* **4,** 1808 (2013).
8. Meier, D. *et al*. Anisotropic conductance at improper ferroelectric domain walls. *Nat. Mater.* **11,** 284–288 (2012).
9. Wu, W., Horibe, Y., Lee, N., Cheong, S.-W. & Guest, J. R. Conduction of topologically protected charged ferroelectric domain walls. *Phys. Rev. Lett.* **108,** 077203 (2012).
10. Oh, Y. S., Luo, X., Huang, F.-T., Wang, Y. & Cheong, S.-W. Experimental demonstration of hybrid improper ferroelectricity and the presence of abundant charged walls in $(Ca,Sr)_3Ti_2O_7$ crystals. *Nat. Mater.* **14,** 407–413 (2015).
11. Eliseev, E. A., Morozovska, A. N., Svechnikov, G. S., Gopalan, V. & Shur, V. Y. Static conductivity of charged domain walls in uniaxial ferroelectric semiconductors. *Phys. Rev. B* **83,** 235313 (2011).
12. Gureev, M. Y., Tagantsev, A. K. & Setter, N. Head-to-head and tail-to-tail 180° domain walls in an isolated ferroelectric. *Phys. Rev. B* **83,** 184104 (2011).
13. Ma, E. Y. *et al*. Mobile metallic domain walls in an all-in-all-out magnetic insulator. *Science* **350,** 538–541 (2015).
14. Campbell, M. P. *et al*. Hall effect in charged conducting domain walls. *Nat. Commun.* **7,** 13764 (2016).
15. Tselev, A. *et al*. Microwave a.c. conductivity of domain walls in ferroelectric thin films. *Nat. Commun.* **7,** 11630 (2016).
16. Ruff, E. *et al*. Conductivity contrast and tunneling charge transport in the vortex-like ferroelectric domain pattern of multiferroic hexagonal $YMnO_3$. *Phys. Rev. Lett.* **118,** 036803 (2017).
17. Schaab, J. *et al*. Imaging and characterization of conducting ferroelectric domain walls by photoemission electron microscopy. *Appl. Phys. Lett.* **104,** 232904 (2014).
18. Schaab, J. *et al*. Contact-free mapping of electronic transport phenomena of polar domains in $SrMnO_3$ thin films. *Phys. Rev. Appl.* **5,** 054009 (2016).
19. Kalashnikova, A. M. & Pisarev, R. V. Electronic structure of hexagonal rare-earth manganites $RMnO_3$. *JETP* **78,** 143–147 (2003).
20. Chae, S. C. *et al*. Direct observation of the proliferation of ferroelectric loop domains and vortex-antivortex pairs. *Phys. Rev. Lett.* **108,** 167603 (2012).
21. Zhang, Q. H. *et al*. Direct observation of interlocked domain walls in hexagonal $RMnO_3$ ($R=$ Tm, Lu). *Phys. Rev. B* **85,** 020102(R) (2012).
22. Kumagai, Y. & Spaldin, N. A. Structural domain walls in polar hexagonal manganites. *Nat. Commun.* **4,** 1540 (2012).
23. Choi, T. *et al*. Insulating interlocked ferroelectric and structural antiphase domain walls in multiferroic $YMnO_3$. *Nat. Mater.* **9,** 253–258 (2010).
24. Skjærvø, S. H. *et al*. Interstitial oxygen as a source of p-type conductivity in hexagonal manganites. *Nat. Commun.* **7,** 13745 (2016).
25. Yan, Z. *et al*. Growth of high-quality hexagonal $ErMnO_3$ single-crystals by the pressurized floating-zone method. *J. Cryst. Growth* **409,** 75–79 (2015).
26. Crassous, A., Sluka, T., Tagantsev, A. K. & Setter, N. Polarization charge as a reconfigurable quasi-dopant in ferroelectric thin films. *Nat. Nanotech.* **10,** 614–618 (2015).
27. Mundy, J. A. *et al*. Visualizing the interfacial evolution from charge compensation to metallic screening across the manganite metal–insulator transition. *Nat. Commun.* **5,** 3464 (2014).
28. Coeuré, Ph., Guinet, F., Peuzin, J. C., Buisson, G. & Bertaut, E. F. Ferroelectric properties of hexagonal orthomanganites of yttrium and rare earths. *Proc. Int. Meet. Ferroelectr.* **1,** 332–340 (1966).
29. Medvedeva, J. E., Anisimov, V. I., Korotin, M. A., Mryasov, O. N. & Freeman, A. J. The effect of Coulomb correlation and magnetic ordering on the electronic structure of hexagonal phases of ferroelectromagnetic $YMnO_3$. *J. Phys. Condens. Matter* **12,** 4947–4958 (2000).
30. Van Aken, B. B., Palstra, T. T. M., Filippetti, A. & Spaldin, N. A. The origin of ferroelectricity in magnetoelectric $YMnO_3$. *Nat. Mater.* **3,** 164–170 (2004).
31. Rahmanizadeh, K., Wortmann, D., Bihlmayer, G. & Blügel, S. Charge and orbital order at head-to-head domain walls in $PbTiO_3$. *Phys. Rev. B* **90,** 115104 (2014).
32. *Fundamentals of Power Electronics* (eds Erickson, R. W. & Maksimovic, D.) 2nd edn (Springer Science + Business Media, LLC, 2001).

## Acknowledgements

We thank M. Fiebig for direct financial support and scientific input, and M. Trassin and A. Kaiser for fruitful discussions. We thank HZB for the allocation of synchrotron beam time and we gratefully acknowledge financial support by HZB. D.M., J.S. and N.A.S. acknowledge funding from the ETH Zurich and the SNF (proposal no. 200021_149192, D.M. and J.S.), the Alexander von Humboldt Foundation (D.M.) and the ERC Advanced Grant programme (grant number 291151, N.A.S.). Electron microscopy research at Cornell (J.A.M., M.E.H., D.A.M. and D.G.S.) was supported by the U.S. Department of Energy, Office of Basic Energy Sciences, Division of Materials Sciences and Engineering under Award no. DE-SC0002334. This work made use of the electron microscopy facility of the Cornell Center for Materials Research (CCMR) with support from the National Science Foundation Materials Research Science and Engineering Centers (MRSEC) programme (DMR-1120296) and NSF IMR-0417392. We gratefully acknowledge the use of facilities with the LeRoy Eyring Center for Solid State Science at Arizona State University and assistance from J. Mardinly and T. Aoki. J.A.M. acknowledges financial support from the Army Research Office in the form of a National Defense Science & Engineering Graduate Fellowship and from the National Science Foundation in the form of a National Science Foundation Graduate Research Fellowship. M.S. was supported by MINECO-Spain through Grants No. FIS2013-48668-C2-2-P and No. SEV-2015-0496, and Generalitat de Catalunya (2014 SGR301). E.B. and Z.Y. were supported in part by the US Department of Energy and carried out at the Lawrence Berkeley National Laboratory under Contract No. DE-AC02-05CH11231.

## Author contributions

J.A.M. and M.E.H. conducted and analysed the EELS measurements, assisted by R.H., under supervision of D.A.M. and D.G.S. Y.K., M.S. and N.A.S. performed the semiclassical and DFT calculations. J.S. performed the cAFM measurements under supervision of D.M. The analysis in terms of X-PEEM was provided by I.P.K., J.S., D.M.G., H.D., C.M.S. and D.M.; Z.Y., E.B. and R.R. allocated the samples. A.C. and D.M. developed the concept of electric-field gating. D.M. initiated and coordinated this project, and wrote the manuscript supported by J.A.M., J.S., Y.K., M.S., A.C. and N.A.S.

## Additional information

Supplementary information is available in the online version of the paper. Reprints and permissions information is available online at www.nature.com/reprints. Publisher's note: Springer Nature remains neutral with regard to jurisdictional claims in published maps and institutional affiliations. Correspondence and requests for materials should be addressed to D.M.

## Competing financial interests

The authors declare no competing financial interests.



© 2017 Macmillan Publishers Limited, part of Springer Nature. All rights reserved.

## Methods

**Spectroscopy.** $ErMnO_3$ platelets were oriented by Laue diffraction such that the specimen would be imaged down the [100] zone axis of the crystal in TEM. Cross-sectional TEM samples were prepared using an FEI Strata 400 Focused Ion Beam with a final milling step of 2 keV to minimize surface damage. The TEM specimens were imaged on a 100 keV Nion UltraSTEM optimized for EELS imaging (30 mrad convergence angle, 130 pA of usable beam current, ~1 Å spatial resolution). The microscope was equipped with a Gatan Quantum Dual EELS spectrometer; EELS spectra were collected with a 0.1 eV $pixel^{-1}$ dispersion resulting in 0.3 eV energy resolution. Fine-structure information from the O K edge and Mn $L_{2,3}$ edge was collected simultaneously with the ADF signal. Gain and dark noise were corrected using Digital Micrograph. Four cross-sectional TEM specimens were prepared from two distinct $ErMnO_3$ platelets (within the platelets the sample locations were separated by millimetres). Multiple distinct domain walls were identified in each TEM specimen each separated by several micrometres. In sum, over a dozen domain walls were analysed. Post-acquisition, an off-line drift correction was performed to correct the small sample drift ($<0.5$ Å $min^{-1}$). The Mn $L_{2,3}$ fine structure was analysed following a standard power-law background subtraction from approximately 10 eV prior to the edge onset. No additional noise reduction algorithms were employed to avoid artefacts. Scanning was performed in rapid succession perpendicular to the wall orientation so that each scan included signal from across the wall as well as the reference regions on either side. Signals were binned perpendicular to the scan direction to produce a single line scan through the wall. Manganese positions were identified from the integrated signal intensity; the signal was then summed over each manganese position to produce a single spectrum from each row of manganese atoms in the spectrum image. Averaging over manganese positions increased the signal to noise for the EELS analysis.

**Model calculations.** In our semiclassical model of the carrier redistribution at the charged domain walls, we treat the bulk material as a p-type semiconductor using the calculated density of states and values of $P = 7.1\ \mu C\ cm^{-2}$ and $\varepsilon = 13$ (ref. 33) extracted from DFT calculations of bulk $YMnO_3$. The domain walls are introduced as charged planes, with a surface charge density equal to $\pm 2P_z$. The equilibrium distribution of screening carriers is calculated by iteratively solving the Poisson equation of a one-dimensional system with two isolated domain walls. The local carrier density is determined at each step by integrating the bulk density of states to the trial Fermi level, and by enforcing the condition of overall charge neutrality.

**Density functional theory.** First-principles calculations were performed using the projector augmented-wave method[34] as implemented in VASP[35]. PAW data sets with radial cutoffs of 1.48, 1.22 and 0.80 Å for Y, Mn and O, respectively, were employed. The exchange–correlation interactions between electrons were treated using the local density approximation with Hubbard $U$ correction[36,37]. The $U$ and $J$ parameters on the Mn $3d$ orbitals were set to 5 and 0.88 eV, respectively. The $P6_3cm$ noncollinear magnetic configuration of $YMnO_3$, which gives a bandgap of 1.8 eV close to the experimental gap of 1.6 eV (ref. 19), was adopted. Lattice constants and internal positions were fully relaxed until the stress and forces acting on all atoms converged to less than 0.02 GPa and 0.005 eV Å, respectively. The cutoff energy was set to 550 eV, and a $\Gamma$ centred $4 \times 4 \times 2$ $k$-point sampling for the reciprocal space integration was employed. The projected densities of states were evaluated within the spheres centred on the atomic sites with radii of 1.82, 1.32 and 0.82 Å for Y, Mn and O, respectively. For the calculations of polarons, the lattice constants were fixed to the values of the relaxed unit cell, and a $\Gamma$ centred $2 \times 2 \times 2$ $k$-point sampling was adopted. The local symmetry was reduced by moving the apical oxygen ions away from the Mn ion by 0.2 Å so that an electron can easily be captured to the Mn $d_{z^2}$ orbital. Y ions were not moved in the initial structure, but they were spontaneously relaxed to the lowest energy positions via structure optimization. Relative energies between the polaronic and itinerant Bloch electrons were calculated for $2 \times 2 \times 1$ supercells composed of 120 atoms as a function of the $U$ parameter, with $J$ fixed at 0.88 eV. For itinerant electrons, band-filling corrections were applied. To remove the spurious electrostatic energy caused by the finite background charge, we adopted the scheme of ref. 38.

**Data availability.** The data that support the findings of this study are available from the authors on reasonable request.

## References

33. Stengel, M., Fennie, C. J. & Ghosez, P. Electrical properties of improper ferroelectrics from first principles. *Phys. Rev. B* **86,** 094112 (2012).
34. Blöchl, P. E. Projector augmented-wave method. *Phys. Rev. B* **50,** 17953–17979 (1994).
35. Kresse, G. & Furthmüller, J. Efficient iterative schemes for *ab initio* total-energy calculations using a plane-wave basis set. *Phys. Rev. B* **54,** 11169–11186 (1996).
36. Perdew, J. P. & Zunger, A. Self-interaction correction to density-functional approximations for many-electron systems. *Phys. Rev. B* **23,** 5048–5079 (1981).
37. Liechtenstein, A. I., Anisimov, V. I. & Zaanen, J. Density-functional theory and strong interactions: orbital ordering in Mott–Hubbard insulators. *Phys. Rev. B* **52,** R5467–R5470 (1995).
38. Kumagai, Y. & Oba, F. Electrostatics-based finite-size corrections for first-principles point defect calculations. *Phys. Rev. B* **89,** 195205 (2014).



© 2017 Macmillan Publishers Limited, part of Springer Nature. All rights reserved.